

1 **Multichannel Analysis of Surface Waves (MASW) for the**
2 **internal characterisation of the Flüela rock glacier:**
3 **overcoming the limitations of seismic refraction tomography**

4 Ilaria Barone¹, Alexander Bast^{2,3}, Mirko Pavoni¹, Steven Javier Gaona Torres¹, Luca Peruzzo¹
5 and Jacopo Boaga¹

6 ¹ Department of Geosciences, University of Padova, Padua, Italy

7 ² WSL Institute for Snow and Avalanche Research SLF, Permafrost Research Group, Davos Dorf, Switzerland

8 ³ Climate Change, Extremes and Natural Hazards in Alpine Regions Research Center CERC, Davos Dorf,
9 Switzerland

10 *Correspondence to:* Ilaria Barone (ilaria.barone@unipd.it) and Mirko Pavoni (mirko.pavoni@unipd.it)

11 **Abstract.** A multi-method geophysical campaign was carried out to characterize the subsurface of the Flüela rock
12 glacier, Grisons, Switzerland, using electrical resistivity tomography (ERT), seismic refraction tomography (SRT)
13 and multichannel analysis of surface waves (MASW). Surface wave analysis is not commonly used in mountain
14 permafrost environments, although it could be applied to any dataset acquired for conventional SRT analysis if
15 collected with low-frequency geophones. Here, we show that the use of the MASW method can be efficiently
16 applied to highlight the presence of an ice-bearing layer, thus overcoming potential limitations of the common
17 SRT analysis in these environments, such as tackling velocity inversions at depth or identifying layers which are
18 invisible due to the lack of head wave arrivals. Our results are corroborated by synthetic models that simulate the
19 propagation of seismic waves in a mountain permafrost environment with changing ice and water contents.

20
21 Keywords: multichannel analysis of surface waves (MASW); electrical resistivity tomography (ERT); seismic
22 refraction tomography (SRT); mountain permafrost hydrology; rock glacier hydrology; ground ice content.

23 **1 Introduction**

24 The warming and degradation of European mountain permafrost (PERMOS, 2020; Noetzli et al., 2024) facilitates
25 the formation and dynamics of alpine mass movements such as rock falls, landslides or debris flows (Arenson and
26 Jakob, 2014; Kofler et al., 2021; Bast et al., 2024a; Jacquemart et al., 2024), and hence, may impact human safety
27 and infrastructure (Arenson and Jakob, 2017; Duvillard et al., 2019). Consequently, in densely populated
28 mountain regions such as the European Alps, there is a significant demand for reliable tools to map and
29 characterise permafrost environments, accurately assess associated risks, and apply practical solutions for the
30 construction and maintenance of durable infrastructure (e.g., Bommer et al., 2010).

31 Rock glaciers are common, widespread, often tongue-shaped debris landforms found in periglacial mountain
32 environments containing ice, rocks, air and water (Kellerer-Pirklbauer et al., 2024; Haeberli et al., 2006;

33 RGIK, 2022). They form in the deposition zones of snow avalanches and rock fall (Kenner et al. 2019) and
34 develop over centuries to millennia (Krainer et al., 2015; Haeberli et al., 1999) due to past or ongoing creep
35 (RGIK, 2022), resulting from internal deformation within the ground ice and shearing at distinct horizons
36 (Arenson et al., 2002; Cicoira et al., 2021). In the past two decades, the creep rate of rock glaciers has generally
37 increased, and this is often linked to climate change (Kellerer-Pirkelbauer et al., 2024; PERMOS 2020, Hu et al.
38 2025).

39 Rock glaciers have primarily been studied from geomorphological, climatic, and kinematic perspectives, with less
40 focus on their hydrological aspects (e.g., Bast et al., 2024b; Cicoira et al., 2019; Haeberli et al., 2006; Hu et al.,
41 2025; Kellerer-Pirkelbauer et al., 2024; Kenner et al., 2020), as also highlighted by recent reviews by Arenson et
42 al. (2022) and Jones et al. (2019). This gap in understanding arises because of the complexity of the distribution
43 of ice and water in rock glaciers. The relation between rock glacier kinematics and their hydrology is also complex,
44 influenced by factors such as variable surface cover and groundwater flow, which affect infiltration rates, heat
45 transfer and reaction times (Arenson et al., 2022). Nevertheless, understanding rock glacier hydrology is essential
46 to comprehend rock glacier velocities, i.e. kinematics, and their potential impacts on alpine mass movements.

47 Water can exist within rock glaciers as seasonally frozen in the active layer, as perennially frozen ice in the
48 permafrost body, or perennially unfrozen in liquid form in taliks. Permafrost primarily influences water flow paths
49 by acting as a physical barrier that restricts movement (Arenson et al., 2022). Conceptual models (Giardino et al.,
50 1992), alongside geochemical (Krainer and Mostler, 2002; Krainer et al., 2007) and geophysical studies (Pavoni
51 et al., 2023a), suggest that a continuous ice-rich frozen layer functions as an aquiclude, separating supra-
52 permafrost flow caused by snow and ice melt, as well as precipitation, from a deeper sub-permafrost flow (Jones
53 et al. 2019). However, the stratigraphy and the bedrock under rock glaciers are often very heterogeneous over
54 short distances, complicating the hydrology (Bast et al., 2024b; Boaga et al., 2020). The thermal state of the
55 ground also plays a critical role, as liquid water can exist below 0°C due to factors such as water salinity, high
56 clay content, or pressure (Arenson et al., 2022; Arenson and Sego, 2006; Bast et al., 2024b; Williams, 1964). This
57 affects the unfrozen water content and hydraulic conductivity and may lead to intra-permafrost flow, confined
58 water layers or water pockets. Furthermore, heat transport by flowing water can facilitate thawing in specific
59 regions, for instance, leading to the development of taliks (Arenson et al., 2022).

60 Although boreholes provide the most accurate information on the internal structure of rock glaciers (Arenson et
61 al., 2002) and allow the monitoring of subsurface properties through specialised sensors such as high-accuracy
62 piezoresistive level probes with temperature sensors or inclinometers (Bast et al., 2024b; Phillips et al., 2023;
63 Arenson et al., 2002), they only offer point data, they are expensive and are challenging to install in high mountain
64 environments. Geophysical methods are, therefore, often used to achieve a more detailed characterisation of the
65 subsurface and a spatial extent (e.g., Scott et al., 1990; Hauck and Kneisel, 2008).

66 Among the different geophysical techniques, electrical resistivity tomography (ERT) and seismic refraction
67 tomography (SRT) methods are widely used to estimate the structure and internal composition of rock glaciers
68 (Wagner et al., 2019; Pavoni et al., 2023b; Hauck et al., 2011). Also single-station passive seismic methods such
69 as HVSR (Horizontal-to-Vertical Spectral Ratio) are increasingly popular for permafrost characterization and
70 monitoring (Kula et al. 2018), including in rock glacier environments (Guillemot et al. 2020, Guillemot et al.
71 2021, Colombero et al. 2025). Among the advantages of passive seismic methods there is the simplified logistics,
72 which is counterbalanced by the point-station character of the measurement and the lack of high frequencies,

73 resulting in a reduced sensitivity in the very near surface. On the other hand, the multichannel analysis of surface
74 waves (MASW; Park et al., 1999), commonly applied for civil engineering purposes (Park et al., 2018; Olafsdottir
75 et al., 2024) and recently used in permafrost studies in Arctic regions (Glazer et al. 2020, Liu et al. 2022, Tourei
76 et al. 2024), has rarely been applied in mountain permafrost environments (Guillemot et al., 2021; Kuehn et al.,
77 2024). Nevertheless, a seismic shot gather acquired with low-frequency vertical geophones (e.g., with a 4.5 Hz
78 natural frequency) not only records the first arrivals of direct and refracted P-waves but also Rayleigh waves,
79 whose propagation is mainly sensitive to S-wave velocities (Vs). Thus, the application of the MASW method can
80 potentially allow the retrieval of a Vs profile (Socco et al., 2010), complementing the SRT method, which typically
81 focuses on P-wave velocities (Vp). The MASW method offers several advantages over the SRT technique: i) it
82 can reveal velocity inversions in the subsurface, such as a lower velocity layer between two higher velocity layers,
83 ii) the retrieved S-wave velocities are insensitive to the liquid phase present in the medium, and iii) it can provide
84 quantitative information regarding the subsurface mechanical properties like the shear modulus and Young's
85 modulus, for geotechnical characterisation (Park et al., 2007).

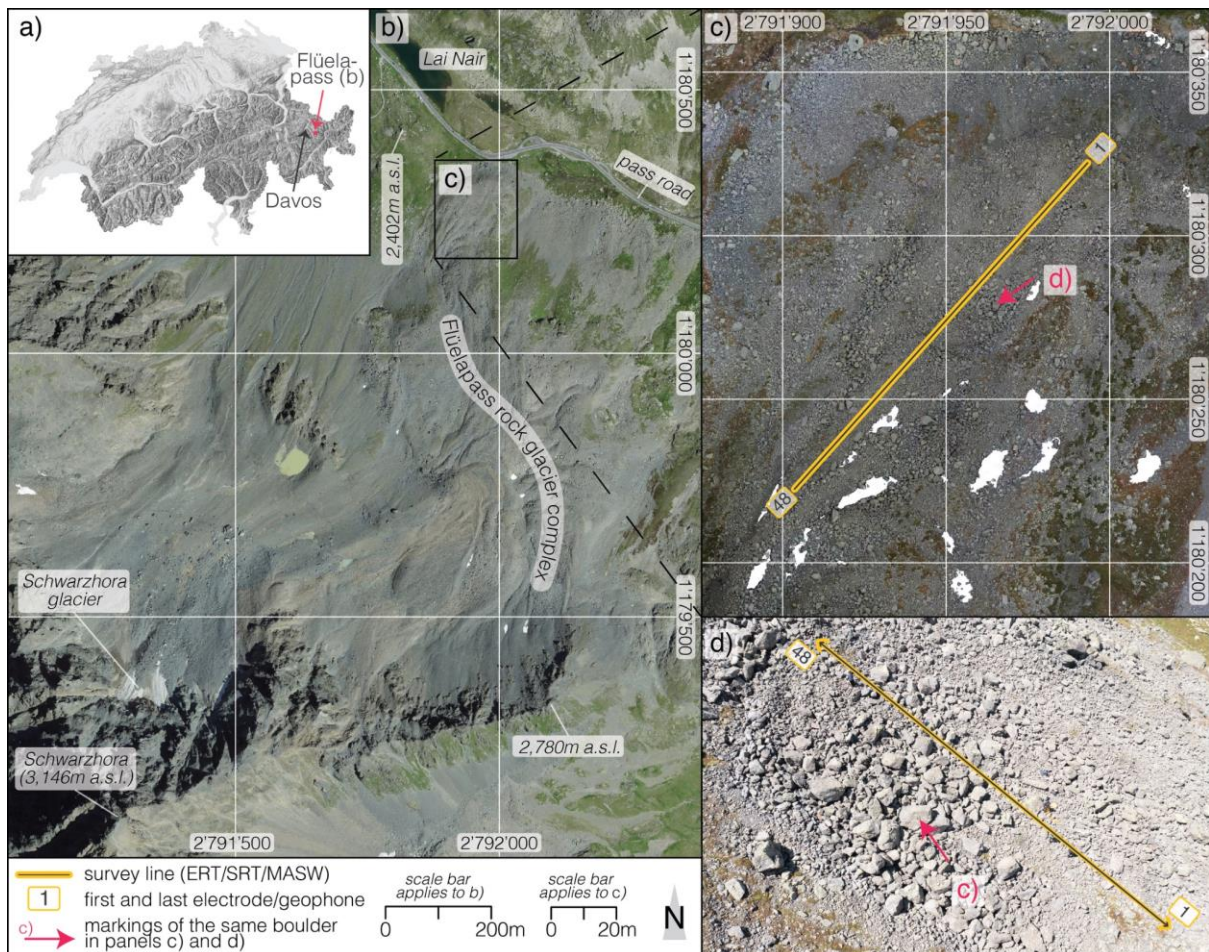
86 In this study, we applied the MASW method along a seismic line that was acquired next to an ERT line at the
87 Flüela rock glacier, Grisons, Switzerland. ERT suggests the presence of an ice-bearing layer in the upper part of
88 the rock glacier tongue, which disappears towards the front. The SRT analysis clearly detects the basal bedrock
89 but surprisingly does not reveal the typical P-wave velocities of the ice-bearing layer. In fact, the SRT results
90 suggest the typical Vp values of liquid water, thus masking the presence of the ice-bearing layer. On the other
91 hand, the Vs models obtained from the MASW results are in very good agreement with the ERT findings.
92 Therefore, we hypothesise the presence of a thin water-saturated sediment layer atop the ice-bearing layer (supra-
93 permafrost flow), which would inhibit the penetration of P-waves. To support our hypothesis, we carried out a
94 full-wave forward modelling and produced synthetic shot gathers. Subsequently, we compared synthetic with
95 field data, both in terms of surface wave dispersion and P-wave first-arrival times.

96 **2 Study site and data acquisition**

97
98 The lower lobe of the Flüelapass rock glacier complex (referred to here as the Flüela rock glacier; 46.746° N,
99 9.951° E) is located in the Eastern Swiss Alps, next to the Flüelapass road in the Community of Zernez, Grisons,
100 at the top of the mountain pass (Figs. 1a and 1b). The active rock glacier, ranging from 2380-2500 m asl., is
101 nourished by the surrounding steep rock walls, which are composed of amphibolite and paragneiss
102 (Bast et al., 2025). The lower investigated tongue of the rock glacier (Fig. 1c) creeps downwards with surface
103 velocities ranging between ~ 10 and ~ 30 cm/year (R. Kenner, SLF, personal communication, based on annual
104 terrestrial laser scans, 2024). The surface material consists of rock debris and boulders of various sizes, along with
105 smaller isolated patches of finer sediments and sparse vegetation (Figs. 1c and 1d).

106 A first study of the Flüela rock glacier by Haeberli (1975) applied refraction seismics to investigate the presence
107 of ground ice. The seismic profiles obtained indicated permafrost at around 10 m depth in the rock glacier front
108 and ice-rich ground below approximately 4 m towards the central lower area of the rock glacier. More recent
109 geophysical research by Boaga et al. (2024) and Bast et al. (2025) confirmed the presence of the ice-bearing layer.
110 Research on permafrost distribution and evolution at the Flüelapass primarily concentrated on a talus slope located

111 approximately 500 m west-northwest, where two boreholes were drilled in 2002 (Lerjen et al., 2003; Phillips et
 112 al., 2009; Kenner et al., 2017). As for the lower tongue investigated here, no borehole information is available.
 113



114
 115 **Figure 1: (a) Location of the Flüela rock glacier complex in Switzerland. (b) Aerial image of the Flüelapass featuring**
 116 **the Flüela rock glacier complex, with markers for orientation (summit, lake, road) and elevation points. (c) A zoomed-**
 117 **in drone ortho mosaic (flight date 28 June 2023) of the investigated lower lobe of the rock glacier complex, highlighting**
 118 **the survey line (electrical resistivity and seismic data, yellow-grey line). The red arrow indicates the same boulder as**
 119 **in the oblique drone image (d). The drone image reveals the coarse and rough surface within the middle section of the**
 120 **survey line (please note that the survey line extends further NW and SW). Basemaps in a) SwissAlti3D multidirectional**
 121 **hillshade and b) SwissImage (flight year 2022) are provided by swisstopo (<https://map.geo.admin.ch>). Note that the**
 122 **legend and North arrow applies to all map sections (a-c).**

123 On 03 August 2024, we collected both electrical resistivity tomography (ERT) and seismic data on the rock
 124 glacier. The measurements were collected along a line of approximately 133 m in the middle of the lobe (Figs. 1c
 125 and 1d). For data collection, we used 48 electrodes for the ERT and 48 geophones for the seismics, with a spacing
 126 of 3 m. We measured all electrode/geophone positions with a Stonex S800 GNSS instrument (Stonex, Paderno
 127 Dugnano, Italy; www.stonex.it) to obtain a detailed topographic profile along the survey line.
 128 The ERT dataset was collected with a Syscal Pro Switch 48 resistivity meter (IRIS Instruments, Orléans, France;
 129 www.iris-instruments.com). This was done with a dipole-dipole multi-skip acquisition scheme
 130 (Pavoni et al., 2023a), with reciprocal measurements and stacking ranging from 3 to 6 (Day-Lewis et al., 2008),

131 for a total of 3542 measured data points. To ensure a good galvanic coupling, i.e., optimal contact resistances, and
132 to obtain a high-quality dataset (Pavoni et al., 2022), conductive textile sachets, wet with salt water, were used as
133 electrodes (Buckel et al., 2023; Bast et al., 2025).

134 The seismic data were collected with two Geode seismographs (Geometrics, San Jose, USA;
135 <http://www.geometrics.com>), using vertical low-frequency geophones with a natural frequency of 4.5 Hz and a
136 20 kg sledgehammer as a seismic source. The source was moved from the first to the last geophone with a distance
137 of six metres between each position, resulting in a total of 24 acquisition positions. At each position, the shot was
138 repeated twice to stack the seismograms and enhance the signal-to-noise ratio.

139 3 MASW Method

140 Surface waves are seismic waves that travel along the Earth's surface, characterised primarily by dispersion, i.e.,
141 different frequencies propagate at different velocities (Everett, 2013). By analysing surface wave dispersion, it is
142 possible to infer different mechanical properties of the medium through which the surface waves propagate (Socco
143 et al., 2010). The depth of investigation of surface waves is associated with the seismic wavelength; a general rule
144 of thumb is to consider one-third to one-half of the seismic wavelength of the lowest frequency component as the
145 maximum penetration depth (Foti et al., 2015). Surface waves are also characterised by multi-modal propagation,
146 meaning they can propagate in multiple modes simultaneously, including the fundamental mode and higher-order
147 modes. The fundamental mode is the simplest form of wave propagation, with higher sensitivity near the surface,
148 typically showing lower propagation velocities and higher amplitudes. Higher-order modes involve more complex
149 sensitivity patterns with depth, can penetrate deeper layers, and usually exhibit higher velocities and lower
150 amplitudes. However, the energy distribution of surface waves over different modes strongly depends on the
151 subsurface conditions, and if higher modes with significant amplitude are present, special attention must be
152 devoted to identifying the different modes (Boaga et al., 2013).

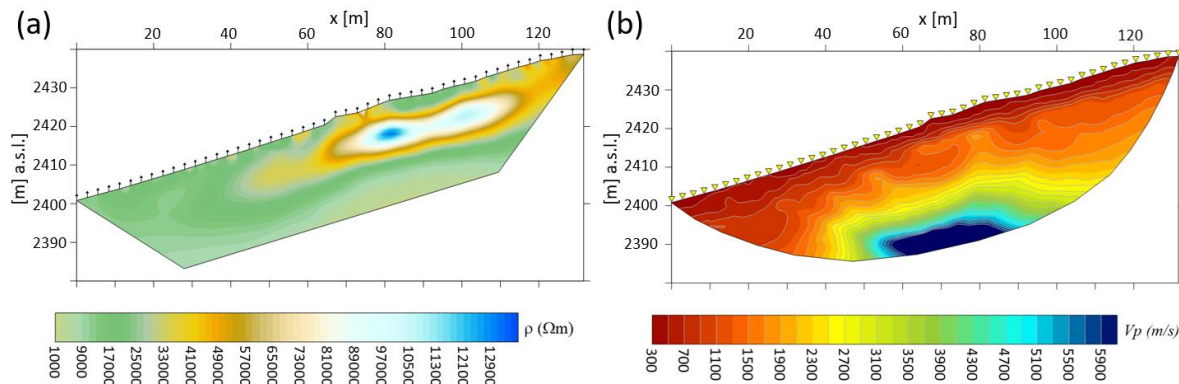
153 Surface wave analysis allows the retrieval of the dispersion relation (phase/group velocity versus frequency). In
154 particular, the Multichannel Analysis of Surface Waves (MASW; Park et al., 1999) uses linear arrays to record
155 the surface wave propagation from an active source in the time-space domain (seismogram). The acquisition setup
156 is identical to SRT, but low-frequency geophones, having typically a natural frequency of 4.5 Hz, are essential
157 for MASW surveys. The seismogram is converted into a frequency-wavenumber (f-k) or frequency-velocity (f-v)
158 spectrum, where the energy maxima corresponding to the different modes are picked. Depth inversion is finally
159 needed to retrieve a 1D Vs profile. Inversion is a non-linear ill-posed problem that can be solved deterministically
160 using the linearized iterative least-squares approach (Herrmann, 1987), or with a stochastic search method, such
161 as the neighbourhood algorithm (Sambridge, 1999). In both cases, some preliminary information is needed to
162 define the starting model (deterministic approach) or the parameter space (stochastic approach).

163 The MASW method assumes homogeneous lateral conditions under the recording array. This condition is hardly
164 met in nature, and when strong lateral heterogeneities are present, the complexity of the resulting spectra could
165 challenge the picking process. For this reason, MASW is sometimes applied using moving windows. In this case,
166 a quasi-2D Vs profile is retrieved, and smooth lateral velocity variations can be identified (Bohlen et al., 2004;
167 Boiero and Socco, 2011). The selection of the moving window length is crucial and requires preliminary testing:
168 a shorter window length causes an increase in lateral resolution but decreases the spectral resolution.

169

170 **4 ERT, SRT and MASW data processing, results and interpretation**171
172 **4.1 ERT and SRT**173
174 The ERT data processing was conducted using the open-source Python-based software *ResIPy*
175 (Blanchy et al., 2020), filtering the quadrupoles with reciprocal and stacking errors exceeding 5 %, which was
176 considered as the expected data error in the inversion modelling (Day-Lewis et al., 2008). The inverted resistivity
177 model (Fig. 2a) was found in two iterations and with a final RMS (Root-Mean Square) misfit of 1.17.178 SRT data processing was performed with two open-source tools. Geogiga Front End Express v. 10.0, from
179 Geogiga Technology Corp. (<https://geogiga.com/products/frontend/>), was used for the picking of first arrivals,
180 while the C++/Python-based library *pyGIMLi* (Rücker et al., 2017) was used for data inversion. In each
181 seismogram, the first-arrival times were picked three times to calculate the standard deviation and define the
182 picking error (1 ms) for the inversion process (Bauer et al., 2010). The inverted P-wave velocity (Vp) model (Fig.
183 2b) was found in five iterations and with a final χ^2 (chi-square) misfit of 1.31.

184

185
186 **Figure 2: (a) The inverted ERT section, after two iterations, has an expected data error of 5% and a final RMS misfit**
187 **of 1.17. The black markers along the surface indicate the positions of the electrodes. (b) The inverted P-wave velocity**
188 **model (SRT), after five iterations, has a picking error of 1 ms and a final χ^2 misfit of 1.31. The yellow triangular**
189 **markers along the surface indicate the positions of the geophones.**190 In the upper 4 - 5 m of the ground, electrical resistivity values are relatively high (~ 20 k Ω m), and Vp values are
191 particularly low (< 600 m/s). This indicates a highly porous layer composed of blocks and debris with low fine
192 sediment content. Towards the front of the rock glacier ($x < 40$ m) and at greater depths, the electrical resistivity
193 decreases (< 10 k Ω m), and the Vp values gradually increase, reaching 1200-1500 m/s at the bottom of the model.
194 Here, the substrate appears more heterogeneous, consisting of a mix of coarse debris and finer sediments. Towards
195 the upper section of the rock glacier lobe, at 4 - 5 m depth, resistivities increase (~ 40 k Ω m) for $40 \text{ m} < x < 60 \text{ m}$,
196 with an even sharper rise to values > 80 k Ω m for $x > 60$ m. These values are typical for an ice-bearing frozen
197 layer (Hauck and Kneisel, 2008). This layer extends to a depth of 10 - 12 m before resistivities clearly decrease
198 to a few k Ω m at the bottom of the model. In the Vp model, values increase at greater depths, with a steep gradient
199 at ~ 20 m depth ($50 < x < 80$ m), where Vp Values reach 6000 m/s, indicating the bedrock. In the upper part of
200 the section, between 4 - 5 m and 10 - 12 m depth, no typical Vp values of an ice-bearing frozen layer are reached
(Vp > 2500 m/s, Hauck and Kneisel, 2008). Therefore, in this area, the ERT and SRT results are inconsistent:

202 while the inverted resistivity model clearly indicates an ice-bearing layer, the Vp model shows a moderate
203 increase, peaking at Vp values \sim 1500 m/s, likely corresponding to a liquid water-saturated layer.

204

205 **4.2 MASW**

206

207 The MASW analysis was performed using a moving window of 24 channels, striking a balance between spatial
208 and spectral resolution. An offset-dependent mute was applied to those shot gathers that presented at least one
209 source bounce as this could significantly impact the subsequent phase measurements. The time of occurrence of
210 the source bounces was automatically identified through the auto-correlation of the near-offset traces. The mute
211 was finally applied to the seismogram to mask the source bounce. Each shot gather was then Fourier transformed
212 in both time and space to obtain the corresponding f-k spectrum, from which the fundamental mode was manually
213 picked. The retrieved dispersion curves were depth inverted using *Dinver* (Wathelet, 2008), an open-source tool
214 included in *Geopsy* (<https://www.geopsy.org/>; last access: 28 February 2025) that performs a stochastic inversion
215 based on the neighbourhood algorithm (Sambridge, 1999). *Dinver* requires the definition of the model space with
216 a fixed number of layers. We used a four-layer model and parameterized each layer with a wide range of seismic
217 velocities and Poisson ratios, while keeping the density constant (Tab. 1). This choice was guided by the
218 preliminary information we gained from ERT and SRT sections, that would indicate two to three layers, depending
219 on the presence of permafrost, and a relatively shallow seismic bedrock. *Dinver* generates a multitude of random
220 models within the model space and calculates for each of these models the misfit between observed and modelled
221 dispersion curves. The final model is characterised by the minimum misfit.

222 **Table 1: Parameter space used for the dispersion curve inversion with the open-source tool *Dinver* (Wathelet, 2008).**

223 **Abbreviations: Vp: P-wave velocities, Vs: S-wave velocities, ρ : density.**

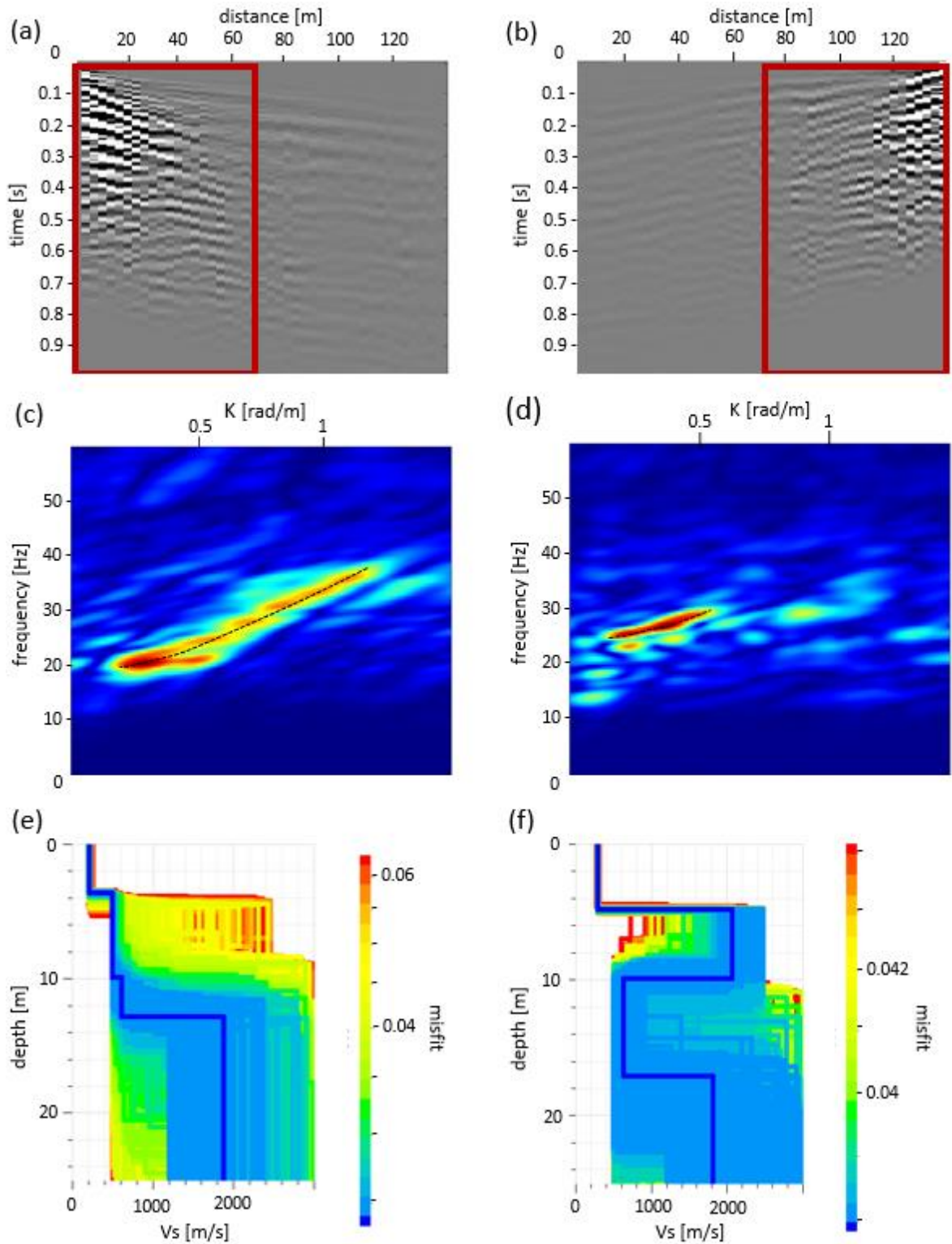
	Thickness [m]	Vp [m/s]	Vs [m/s]	Poisson ratio	ρ [kg/m ³]
1	2 - 12	400 - 1000	200- 500	0.2 - 0.45	1800
2	2 - 12	800 - 5000	500 - 2500	0.2 - 0.45	2000
3	2 - 12	800 - 5000	500 - 2500	0.2 - 0.45	2000
Bedrock	Infinite	2400 - 6000	1200- 3000	0.2 - 0.45	2200

224

225 Figure 3 shows the results of the picking (Figs. 3c and 3d) and the Vs models (Figs. 3e and 3f) derived from the
226 inversion of two dispersion curves. The first curve refers to a shot placed on the left side and the first 24 geophones
227 (Fig. 3a), while the second curve relates to a shot on the right side and the last 24 geophones (Fig. 3b). Despite
228 the noisy character of the seismograms, where strong scattering is observed, the f-k spectra show coherent energy
229 and at least one mode of propagation is clearly recognisable, assumed to be the fundamental mode (Figs. 3c
230 and 3d). The two spectra show different frequency and wavenumber distributions, indicating different subsurface
231 conditions. The maximum penetration depth, which is approximately half of the wavelength, can be computed
232 from the minimum picked frequency, and it is about 15 m. The inversion results reveal a smooth increase of
233 velocity with depth in the left part of the section, i.e., towards the front of the rock glacier (Fig. 3e), while it clearly

234 highlights a shallow (5 m depth) high-velocity layer (2000 m/s) on the right side, i.e., the upper part of the rock
235 glacier (Fig. 3f). The high-velocity layer has a thickness of approximately 5 m. At a depth of 10 m, a clear and
236 sharp decrease in the velocity is observed. Good convergence is reached in the inversion down to the maximum
237 sensitivity of 15 m. Below this depth, results should be treated with caution. The lack of convergence manifests
238 as a wide velocity range with a similar misfit: most models in this depth range are equally plausible. Lower-
239 frequency data is needed to constrain the inversion at greater depths. It is important to note that the limited
240 frequency range characterising the picked dispersion curves is partly due to the loss of high frequency from
241 scattering and partly to the presence of a high-impedance boundary (the top of the bedrock in the left half of the
242 section and the top of the frozen layer on the right) that likely prevents most of the low-frequency energy from
243 penetrating below.

244



245
246 Figure 3: (a) Seismogram (grayscale) of the leftmost shot, where the red rectangle indicates the selected receivers for
247 analysis. The offset-dependent mute effect is visible after 0.7 s, obscuring the source bounce. (c) Frequency-
248 wavenumber (f-k) spectrum of the traces highlighted in (a), with the fundamental mode marked by a black dotted
249 curve. The colours represent the seismic energy (low energy in cold colours / high energy in warm colours). (e) Depth
250 inversion result of the picked dispersion curve, where colours represent different misfit values; the dark blue bold line
251 signifies the final solution model, with a misfit of 0.02416. (b), (d), and (f) correspond to (a), (c), and (e), respectively,
252 but for the rightmost shot. In this case, the misfit of the final solution model is 0.03797.

253 **4.3 Interpretation**

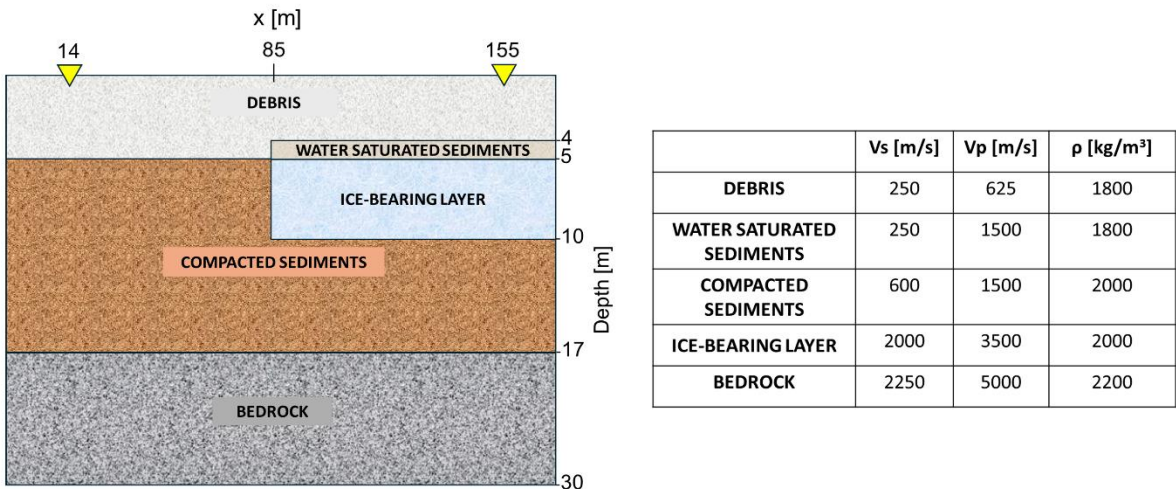
254 The obtained Vs models align well with the inverted resistivity section (Fig. 2a). The Vs values of the shallow
255 (5 - 10 m depth) high-velocity (2000 m/s) layer observed in the right part of the section (Fig. 3f) are indeed
256 consistent with the presence of an ice-bearing permafrost layer (Kuehn et al., 2024) that overlies a lower velocity
257 layer of unfrozen sediments. Conversely, at depths of 5 m and below, the inverted SRT model indicates Vp values
258 that are too low to support this conclusion, with a maximum value of 1500 m/s, which is characteristic of liquid
259 water-saturated sediments. This suggests the presence of a supra-permafrost water layer, which can be commonly
260 found in rock glacier environments where the frozen layer acts as an aquiclude (Krainer et al., 2007;
261 Pavoni et al., 2023; Arenson et al., 2022, Jones et al., 2019). The ERT model does not resolve the presence of a
262 (thin) water-saturated layer given a spacing of 3 m between the electrodes (see the “ERT Synthetic (Forward)
263 Modeling” section in the Supplementary Material), nor does the MASW, which is sensitive to S-waves and thus
264 insensitive to fluids. However, the ~ 1500 m/s P-wave velocities retrieved by the SRT method may indicate the
265 presence of a (thin) water-saturated layer. In fact, such a layer may strongly attenuate body wave transmission
266 and mask further impedance contrasts at depth (Pride et al., 2004). To verify this hypothesis, we performed full-
267 wave (FW) seismic synthetic modelling (Chapter 5).

268 **5 Synthetic data generation and comparison to field data**

269
270 **5.1 Synthetic modelling**

271 To verify the reliability of the obtained results, we generated synthetic seismograms based on a simplified
272 subsurface model derived from the joint interpretation of ERT, SRT and MASW results. Synthetic shot gathers
273 are compared to the real ones in terms of surface waves and first-arrival times.

274 Synthetic seismic data are generated using SW4 3.0 (Petersson and Sjögren, 2023), which solves the seismic
275 wave equations in Cartesian coordinates for 3D heterogeneous media (Sjögren and Petersson, 2012;
276 Zhang et al., 2021). The conceptual model for the simulation is shown in Fig. 4. The left part of the model is
277 characterised by three main layers: (i) a 5 m-thick debris layer, (ii) a 12 m-thick layer of more compacted
278 sediments and (iii) the bedrock. On the right side of the section, we included a 5 m-thick ice-bearing layer, and
279 we hypothesised a 1 m-thick water-saturated layer above it. This model serves as a simplified representation of
280 the assumed real subsurface, where clearly, the shape, thickness, and composition of the different layers are not
281 regular and homogeneous. Moreover, it does not reproduce the small-scale heterogeneities in the model that are
282 beyond the resolution of our field surveys. However, it represents the main structures highlighted by the MASW,
283 ERT and SRT results, with the velocity and thickness of the different layers compatible with the results illustrated
284 in Chapter 4.



286

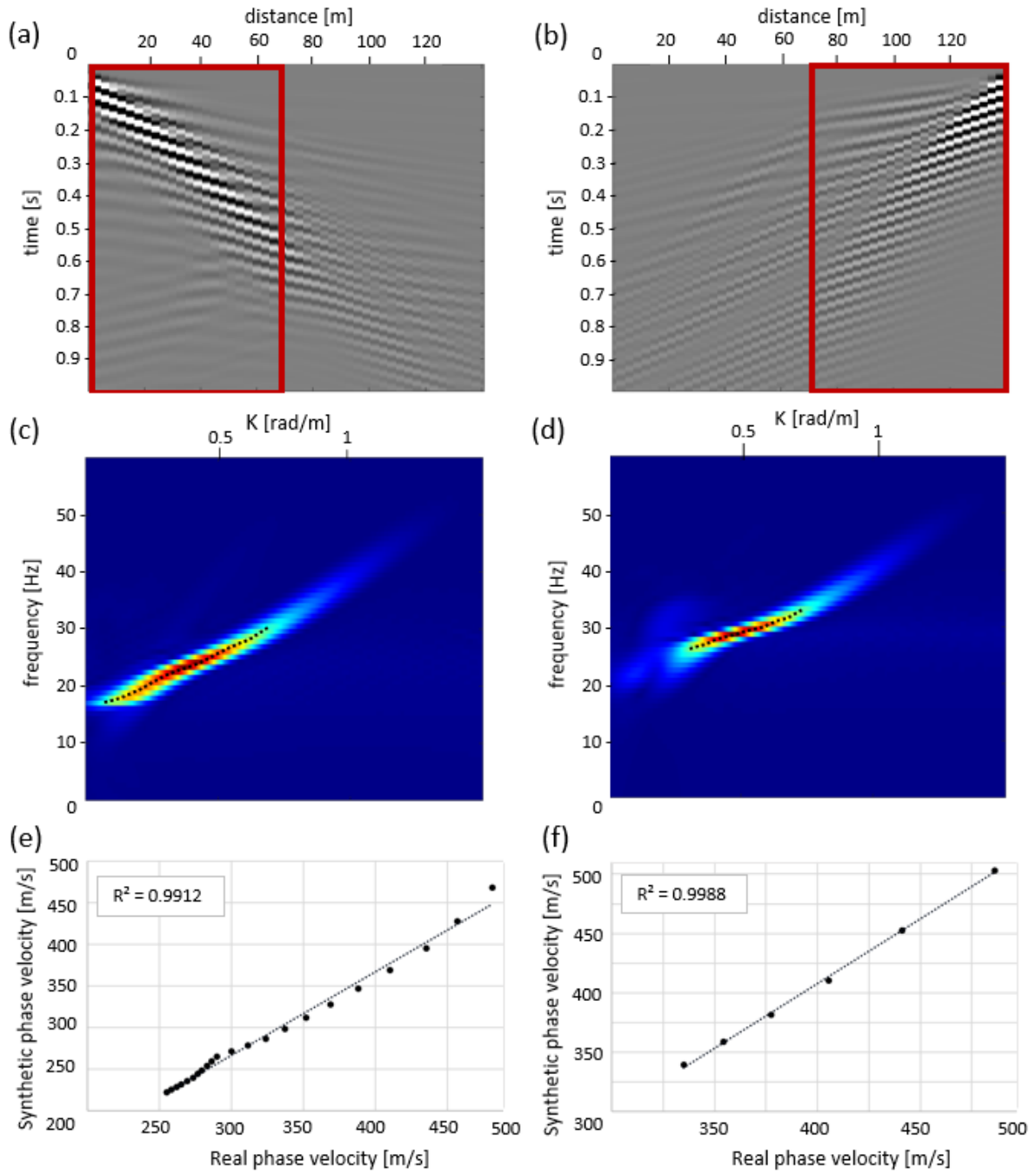
287 **Figure 4: Conceptual model used for the synthetic seismic modelling with the SW4 software (Petersson and Sjögren,**
 288 **2023). The two yellow triangles denote the first and the last geophones in the array. Abbreviations as in Tab. 1.**

289 The simulation domain is 170 x 30 x 30 m in the x, y and z directions. The grid step used was 0.5 m, and the time
 290 step automatic setting was 0.87 ms, to comply with the stability criteria. Absorbing boundaries were included in
 291 the model to prevent the generation of reflections from the model edges, both at its bottom and laterally, while a
 292 free surface condition was set at the top. An array composed of 48 vertical receivers, with a spacing of 3 m, was
 293 placed in the middle of the model ($14 \text{ m} \leq x \leq 155 \text{ m}$, $y = 15 \text{ m}$) to reproduce the real case geometry. The source
 294 was a vertical point load at the surface with a central frequency of 15 Hz. Two simulations were run, corresponding
 295 to a shot on the left side of the array at the location of the first receiver and a shot on the right side at the last
 296 receiver location.

297 **5.2 Comparison between synthetic and field data**

298

299 Figures 5a and 5b show the synthetic shot gathers as grayscale plots. When compared to Figs. 3a and 3b, it is clear
 300 how much noisier the field data are compared to the synthetic ones. This is the effect of scattering caused by the
 301 boulders and coarse debris at the surface of the rock glacier. Consequently, the real f-k spectra (Figs. 3c and 3d)
 302 are also noisier than the synthetic ones (Figs. 5c and 5d). However, the frequency and wavenumber distribution
 303 of the fundamental mode in the modelled data is similar to the field observations. This is confirmed by comparing
 304 the picking of modelled and real spectra (Figs. 5e and 5f). As highlighted in the scatterplots, the phase velocity
 305 values obtained by sampling the fundamental mode in the synthetic spectra show a high correlation with the
 306 corresponding values obtained from the field spectra (R^2 value ~ 0.99). Note that the comparison was made by
 307 considering the phase velocity values obtained in the common frequency range in sampling the field spectrum
 308 (Figs. 3c and 3d) and the synthetic spectrum (Figs. 5c and 5d), i.e., 20-35 Hz on the left side and 25-30 Hz on the
 309 right side.

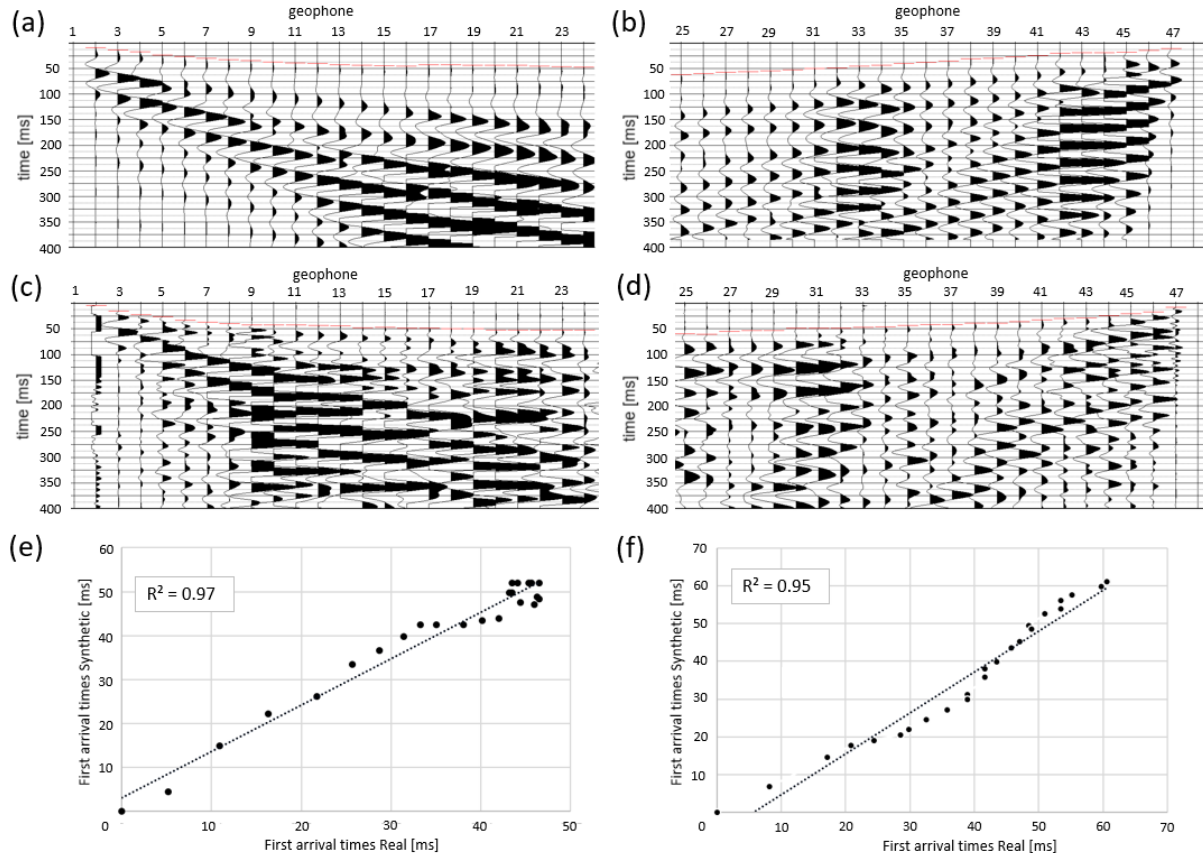


310
311 Figure 5: (a) Synthetic seismogram (grayscale plot) of the left shot, where the red rectangle indicates the selected
312 receivers for analysis. (c) Frequency-wavenumber (f-k) spectrum of the traces highlighted in (a), with the fundamental
313 mode marked by a black dotted curve. (e) Scatterplot of the phase velocity picking obtained from the real (Fig. 3c) and
314 synthetic spectrum (Fig. 5c). The black dotted lines show a simple linear regression line with corresponding R^2 values.
315 (b), (d), and (f) correspond to (a), (c), and (e), respectively, but for the rightmost shot.

316 The modelled first-arrival times are very consistent with the field ones. Figure 6a shows the synthetic shot gathers
317 (in wiggle mode and normalized trace by trace) produced with the source positions at the left side of the geophone
318 array. The synthetic first-arrival times (red lines in Fig. 6a) align with those detected in the field seismogram
319 obtained from the same shot position (Fig. 6c). This is also illustrated by the scatterplot and a high R^2 value (0.97)
320 indicating a high correlation (Fig. 6e). Even considering the source on the right side of the geophone array,

321 synthetic (Fig. 6b) and real (Fig. 6d) shot gathers show very similar first-arrival times (red lines in Figs. 6b and 6d),
 322 as also confirmed by the scatterplot and the high R^2 value (0.95; Fig. 6f). However, in both the synthetic (Fig. 6b)
 323 and the acquired shot gather (Fig. 6d), the slopes of the refractions are compatible with the P-wave velocity of
 324 water ($V_p = 1500$ m/s), even though the synthetic model contains a higher-velocity layer ($V_p = 3500$ m/s)
 325 representing the ice-bearing permafrost (Fig. 4). This supports the hypothesis that a supra-permafrost water-
 326 saturated layer may have prevented the compressional wave transmission in greater depth, hiding refraction
 327 arrivals from deeper impedance contrasts.

328



329

330 **Figure 6: Considering the conceptual model of Fig. 4a, (a) synthetic seismogram of the left shot plotted in wiggle mode**
 331 **(normalized trace by trace) and the picking (red lines in the traces) of first-arrival times for the first 24 traces; (c)**
 332 **field seismogram on the left shot plotted in wiggle mode and the picking (red lines in the traces) of first-arrival times for the**
 333 **first 24 traces; (e) scatterplot of synthetic first-arrival times and field ones for the left shot. The black dotted lines show**
 334 **a simple linear regression line with corresponding R^2 values. (b), (d), and (f) correspond to (a), (c), and (e), respectively,**
 335 **but for the rightmost shot.**

336 The good agreement between synthetic and field data regarding surface wave dispersion and first-arrival times,
 337 demonstrates the validity of the simple conceptual model presented in Fig. 4, which was used for the forward
 338 simulation. However, slight differences in the synthetic and field picking of the fundamental mode and first-arrival
 339 times may relate to the simplification of the synthetic model, which could not account for the highly complex
 340 topography and the small-scale heterogeneities of shape, thickness, and composition in the different layers.

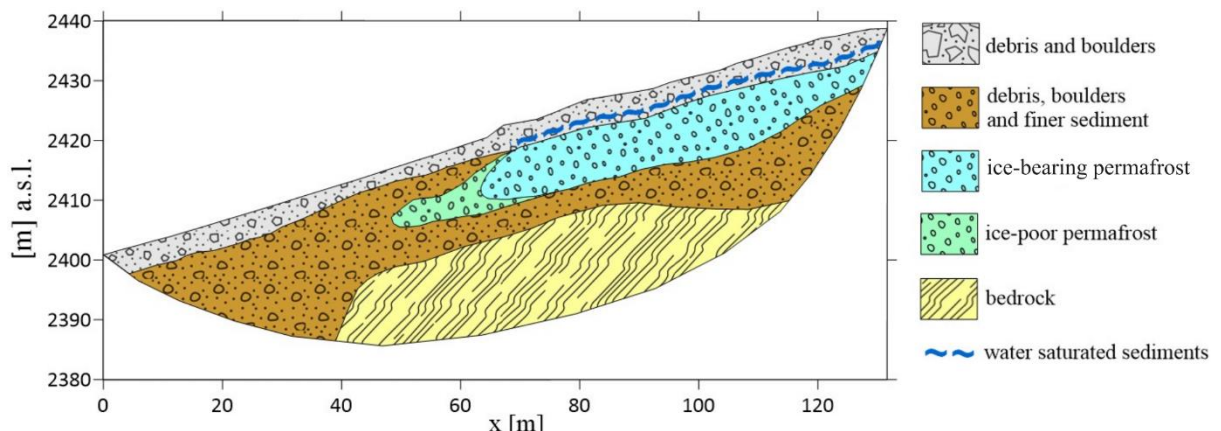
341 **6 Discussion**

342 **6.1 Rock glacier subsurface model and rock glacier hydrology**

343

344 Based on our presented ERT, SRT, MASW field data results, and FW seismic synthetic modelling, we constructed
345 a subsurface model of the Flüela rock glacier (Fig. 7).

346



347

348 **Figure 7: Interpreted subsurface model of the Flüela rock glacier along the geophysical measuring line, derived from**
349 **results of Electrical Resistivity Tomography (ERT), Seismic Refraction Tomography (SRT), Multichannel Analysis of**
350 **Surface Waves (MASW), and Full-Wave (FW) seismic synthetic modelling.**

351 Four main units were identified. The uppermost layer, showing relatively high resistivity values (20 - 40 k Ω m;
352 Fig. 2a) and low seismic velocities ($V_p < 600$ m/s and $V_s \sim 250$ m/s; Fig. 2b and Figs. 3e-f), was interpreted as
353 mainly composed of debris and blocks, with high porosity (air) and poor regarding fine sediments. The deeper
354 unfrozen sediment layer, with lower resistivities (< 10 k Ω m) and relatively higher seismic velocities
355 ($V_p = 1200 - 1500$ m/s and $V_s \sim 500$ m/s), was interpreted as a more heterogeneous compacted layer with both
356 coarse and fine sediments. At the bottom of the model, the presence of bedrock was hypothesized, considering
357 the sharp increase of V_p from 1200 - 1500 m/s to values > 3000 m/s (up to 6000 m/s), and of V_s values from
358 ~ 500 m/s to ~ 2000 m/s at ~ 14 m depth for the left part of the section, and ~ 18 m depth for the right part.
359 Considering that MASW applies a 1D approximation, the V_p model was mainly used to define the bedrock depth
360 spatially. Finally, the high resistivity values (> 80 k Ω m) identified in the right part of the resistivity model between
361 ~ 5 m and ~ 10 m depth, corresponding to a sharp increase of V_s values (up to 2000 m/s), were interpreted as an
362 ice-bearing permafrost layer. It should be noted that the high resistive layer also propagates beyond the middle of
363 the array ($50 < x < 65$ m), but with lower values (~ 40 k Ω m), probably linked to a decrease in the ice content or
364 an increase in temperature.

365 Considering that an ice-rich layer typically acts as an aquiclude (Giardino et al., 1992;
366 Krainer et al., 2007; Pavoni et al., 2023a; Arenson et al., 2022), we hypothesized the presence of a water-saturated
367 layer above the permafrost. The ice-bearing layer is likely not detected in the V_p model because, in SRT studies,
368 the presence of a liquid-saturated layer can obstruct energy transmission in the deeper layers, thereby masking
369 additional impedance contrasts at depth (Carcione and Picotti, 2006; Picotti et al., 2007; Shi et al., 2024). This
370 behaviour was also reproduced in the synthetic seismic data, where the first-arrival times show typical velocities
371 of liquid phases despite the presence of the ice-bearing layer.

372 This hypothesis can be further supported by the presence of a thin layer of fine-to-coarse sediments above a
373 thicker, ice-bearing permafrost layer, as proposed by Boaga et al. (2024). These finer sediments are known to
374 retain more water due to their smaller particle size, particularly if clay or silt is present (Hillel, 2003). However,
375 without ground truthing, particularly drilling, we cannot obtain detailed subsurface information to confirm the
376 exact structure and stratigraphy. Definitive statements regarding the ice and water content or the flow of water
377 within the ice-bearing layer, such as intra-permafrost flow or the presence of taliks, cannot yet be made. Recent
378 drilling in a rock glacier has revealed that areas identified as ice-rich using ERT and SRT methods can also contain
379 significant amounts of liquid water and very fine sediments (personal observations by M. Phillips and A. Bast,
380 SLF, 2024). Combining our methods with additional techniques could provide further insights into the hydrology
381 of rock glaciers in the future. For example, Boaga et al. (2020) demonstrated that highly conductive anomalies in
382 the subsurface, detected using Frequency Domain Electromagnetometry (FDEM) on a rock glacier, can indicate
383 taliks or areas rich in liquid water.

384

385 **6.2 Advancements and challenges in using MASW for rock glacier characterisation**

386

387 Currently, the only two existing examples of MASW used for rock glacier characterisation are those by (i)
388 Guillemot et al. (2021) at the Laurichard rock glacier, France, and (ii) Kuehn et al. (2024) at the Sourdough Rock
389 Glacier, Alaska. However, in the first study, MASW was used in combination with other techniques to constrain
390 a reference model of the unfrozen conditions for mechanical modelling of the rock glacier. In the second study,
391 the aim of the study was to characterise the first few meters of a debris layer, achieved through a high-resolution
392 seismic acquisition with sub-metre geophone spacing. Therefore, to our knowledge, the study presented here is
393 the first successful application of MASW to derive structural information about rock glaciers, particularly
394 concerning the presence of the frozen layer. Indeed, surface wave analysis in periglacial environments is not
395 straightforward. Surface wave penetration depends on the ability to generate low frequencies, which in turn
396 requires heavy sources. The logistical constraints due to the high-mountain environments might hinder this
397 method. Seismic datasets acquired in these contexts are also very noisy due to the scattering produced by debris
398 and boulders and are highly attenuated, which reflects unclear modal distribution and narrow usable frequency
399 bands. The mountainous environment may also affect data quality due to harsh weather conditions, particularly
400 wind, and complex topography. Furthermore, rock glaciers are often highly heterogeneous media that vary
401 significantly in both space and depth; complex 2D/3D structures could generate dispersion images that are difficult
402 to interpret, which challenges data processing and interpretation. For this reason, the choice of the spatial window
403 for the analysis should be made carefully to achieve the best lateral resolution without compromising spectral
404 resolution. In the case of the Flüela rock glacier, the most natural choice was to perform MASW on the lower and
405 upper halves of the line due to the relatively homogeneous conditions on each side. At locations with greater
406 heterogeneity, selecting a suitable window length may be more difficult.

407 **7 Conclusions**

408

409 In this study, we highlighted the potential limitations of the SRT technique in accurately imaging ice-bearing
410 layers in high-mountain rock glaciers, a limitation that may also apply to other permafrost environments. This

411 limitation may particularly arise in cases where a supra-permafrost water-saturated layer exists, acting as a
412 preferential waveguide for seismic refractions and masking the underlying structures. This phenomenon has been
413 observed at the Flüela rock glacier and has been reproduced through a full-wave forward seismic simulation based
414 on a simplified conceptual model. Another well-known limitation of the SRT method is its inability to image
415 velocity inversions in the subsurface, such as an unfrozen sediment layer between the ice-bearing layer and the
416 bottom bedrock.

417 As shown in our study, the surface wave analysis has the potential to overcome both of these limitations. Surface
418 waves can be recorded simultaneously with the collection of seismic refraction data as long as low-frequency
419 geophones are used for the acquisition. The analysis of surface wave dispersion in the frequency-wavenumber
420 ($f - k$) spectrum, followed by the inversion of dispersion curves, enables the retrieval of Vs profiles, which are
421 insensitive to the liquid phase (i.e., they are not affected by the presence of a supra-permafrost water-saturated
422 layer). Moreover, the surface wave dispersion analysis can retrieve velocity inversions in depth and resolve the
423 presence of a low-velocity layer between high-velocity layers. At the Flüela rock glacier, the dispersion images
424 of the left and right sides of the seismic section look different in terms of frequency content and velocity
425 distribution. The Vs profile produced by the inversion of the right-side dispersion curve clearly shows an increase
426 of velocities at 5 m depth, attributed to the ice-bearing layer, and a decrease at about 10 m, compatible with the
427 presence of unfrozen sediments. This demonstrates the effectiveness of MASW for imaging the ice-bearing layer
428 and the underlying unfrozen sediments, even in the presence of a supra-permafrost water layer, as well as the
429 potential to retrieve the thickness of the ice-bearing layer to support the ERT findings.

430 In the future, we plan to implement the MASW technique across various locations, particularly where we have
431 borehole information on the subsurface stratigraphy, to further validate our findings. Additionally, we aim to
432 enhance the surface wave analysis by incorporating passive seismic data, such as ambient seismic noise captured
433 by seismic nodes, to extend our depth of penetration beneath the ice-rich layer to the seismic bedrock.

434 We recommend using low-frequency geophones and appropriate heavy sources whenever possible when
435 collecting SRT profiles. This approach will enable complementary MASW analysis and provide valuable
436 experience, which will undoubtedly benefit mountain permafrost research and enhance our understanding of ice
437 and water content in mountain permafrost, i.e., mountain permafrost hydrology.

438

439 *Data Availability Statement:* The datasets used to obtain the results presented in this work are available at the
440 open-source repository <https://zenodo.org/uploads/14803564>. Furthermore, the ERT datasets will also be included
441 in the International Database of Geoelectrical Surveys on Permafrost (IDGSP).

442 *Author contributing:* IB and MP developed the concept of the study; MP, JB, and AB collected the data; MP
443 performed the data processing of ERT and SRT data; IB and SJGT performed the MASW analysis; all authors
444 contributed to the interpretation of the results, writing and editing of the manuscript.

445 *Competing interests:* The contact author has declared that none of the authors has any competing interests.

446 *Acknowledgements:* The authors want to thank Dr Marcia Phillips for her valuable help and for pre-reviewing the
447 manuscript.

448

449 *Financial support:* The project “Cold spot” is part of the excellence program: “The Geosciences for Sustainable
450 Development” project (Budget Ministero dell’Università e della Ricerca - Dipartimenti di Eccellenza 2023–2027
451 C93C23002690001).

452 **References**

453 Arenson, L., Hoelzle, M., and Springman, S.: Borehole deformation measurements and internal structure of some
454 rock glaciers in Switzerland, *Permafrost and Periglacial Processes*, 13(2), 117–135,
455 <https://doi.org/10.1002/ppp.414>, 2002.

456 Arenson, L., and Jakob, M.: Periglacial geohazard risks and ground temperature increases, *Eng. Geol. Soc.*
457 *Territory*, 1, 233–237, https://doi.org/10.1007/978-3-319-09300-0_44, 2014.

458 Arenson, L.U., and Jakob, M.: Permafrost-related geohazards and infrastructure construction in mountainous
459 environments, *Oxf. Res. Encycl. Nat. Hazard Sci.*, 30, <https://doi.org/10.1093/acrefore/9780199389407.013.292>,
460 2017.

461 Arenson, L. U., and Sego, D. C.: The effect of salinity on the freezing of coarse-grained sands, *Can. Geotech. J.*,
462 43, 325–337, <https://doi.org/10.1139/t06-006>, 2006.

463 Arenson, L. U., Harrington, J. S., Koenig, C. E. M., and Wainstein, P. A.: Mountain Permafrost Hydrology—A
464 Practical Review Following Studies from the Andes, *Geosciences*, 12, 48,
465 <https://doi.org/10.3390/geosciences12020048>, 2022.

466 Bast, A., Bründl, M., and Phillips, M.: CCAMM - A research program for studying the impacts of climate change
467 on mass movements in alpine regions, *Interpraevent 2024. Conference proceedings*, 37–39, 2024a.

468 Bast, A., Kenner, R., and Phillips, M.: Short-term cooling, drying, and deceleration of an ice-rich rock glacier,
469 *The Cryosphere*, 18, 3141–3158, <https://doi.org/10.5194/tc-18-3141-2024>, 2024b.

470 Bast, A., Pavoni, M., Lichtenegger, M., Buckel, J., and Boaga, J.: The use of textile electrodes for electrical
471 resistivity tomography in periglacial, coarse blocky terrain: a comparison with conventional steel electrodes,
472 *Permafrost and Periglacial Processes*, 36(1), 110–122, <https://doi.org/10.1002/ppp.2257>, 2025.

473 Bauer, K., Moeck, I., Norden, B., Schulze, A., Weber, M., and Wirth, H.: Tomographic P wave velocity and
474 vertical velocity gradient structure across the geothermal site Groß Schönebeck (NE German Basin): relationship
475 to lithology, salt tectonics, and thermal regime, *J. Geophys. Res. Solid Earth*, 115, B08312,
476 <https://doi.org/10.1029/2009JB006895>, 2010.

477 Blanchy, G., Saneiyan, S., Boyd, J., McLachlan, P., and Binley, A.: ResIPy, an intuitive open source software for
478 complex geoelectrical inversion/modelling, *Computers & Geosciences*, 137, 104423.
479 <https://doi.org/10.1016/j.cageo.2020.104423>, 2020.

480 Boaga, J., Cassiani, G., Strobbia, C., and Vignoli, G.: Mode misidentification in Rayleigh waves: Ellipticity as a
481 cause and a cure. *Geophysics* 78(4): EN17–EN28, <https://doi.org/10.1190/GEO20120194.1>, 2013.

482 Boaga, J., Phillips, M., Noetzli, J., Haberkorn, A., Kenner, R., and Bast, A.: A comparison of frequency domain
483 electro-magnetometry, electrical resistivity tomography and borehole temperatures to assess the presence of ice
484 in a rock glacier, *Frontiers in Earth Science*, 8, 586430, <https://doi.org/10.3389/feart.2020.586430>, 2020.

485 Boaga, J., Pavoni, M., Bast, A., and Weber, S.: Brief communication: On the potential of seismic polarity reversal
486 to identify a thin low-velocity layer above a high-velocity layer in ice-rich rock glaciers, *The Cryosphere*, 18,
487 3231–3236, <https://doi.org/10.5194/tc-18-3231-2024>, 2024.

488 Bohlen, T., Kugler, S., Klein, G., and Theilen, F.: 1.5D inversion of lateral variation of Scholte-wave dispersion,
489 *Geophysics*, 69, 330344, <https://doi.org/10.1190/1.1707052>, 2004.

490 Boiero, D., and Socco, L.V.: The meaning of surface wave dispersion curves in weakly laterally varying
491 structures, *Near Surface Geophysics*, 9, 561570, <https://doi.org/10.3997/1873-0604.2011042>, 2011.

492 Bommer, C., Phillips, M., and Arenson, L. U.: Practical recommendations for planning, constructing and
493 maintaining infrastructure in mountain permafrost, *Permafrost and Periglacial Processes*, 21, 97–104,
494 <https://doi.org/10.1002/ppp.679>, 2010.

495 Buckel, J., Mudler, J., Gardeweg, R., Hauck, C., Hilbich, C., Frauenfelder, R., Kneisel, C., Buchelt, S., Blöthe, J.
496 H., Hördt, A., and Bücker, M.: Identifying mountain permafrost degradation by repeating historical electrical
497 resistivity tomography (ERT) measurements, *The Cryosphere*, 17(7), 2919–2940, <https://doi.org/10.5194/tc-17-2919-2023>, 2023.

499 Carcione, J. M., and Picotti, S.: P-wave seismic attenuation by slow-wave diffusion: Effects of inhomogeneous
500 rock properties, *Geophysics*, 71(3), O1-O8, <https://doi.org/10.1190/1.2194512>, 2006.

501 Ciccoira, A., Marcer, M., Gärtner-Roer, I., Bodin, X., Arenson, L. U., and Vieli, A.: A general theory of rock
502 glacier creep based on in-situ and remote sensing observations, *Permafrost and Periglacial Processes*, 32(1), 139–
503 153, <https://doi.org/10.1002/ppp.2090>, 2021.

504 Ciccoira, A., Beutel, J., Faillettaz, J., and Vieli, A.: Water controls the seasonal rhythm of rock glacier flow, *Earth
505 and Planetary Science Letters*, 528, 115844, <https://doi.org/10.1016/j.epsl.2019.115844>, 2019.

506 Colombero, C., Di Toro, L., Khosro Anjom, F., Godio, A., and Morra Di Cella, U.: Ambient Seismic Noise and
507 Microseismicity Monitoring of Periglacial Bodies: A Case Study on the Gran Sometta Rock Glacier (NW Italian
508 Alps), *Permafrost and Periglacial Processes*, 0:1–16, <https://doi.org/10.1002/ppp.22862025>, 2025.

509 Day-Lewis, F. D., Johnson, C. D., Singha, K., Lane, J.W.J.: Best practices in electrical resistivity imaging: Data
510 collection and processing, and application to data from Corinna, Maine, EPA Report, Boston, MA, 2008.

511 Duvillard, P. A., Ravanel, L., Marcer, M., and Schoeneich, P.: Recent evolution of damage to infrastructure on
512 permafrost in the French Alps, *Reg. Environ. Change*, 19 (5), 1281–1293, <https://doi.org/10.1007/s10113-019-01465-z>, 2019.

514 Everett, M. E.: *Near-Surface Applied Geophysics*. Cambridge University Press,
515 <https://doi.org/10.1017/CBO9781139088435>, 2013.

516 Foti, S., Lai, C. G., Rix, G. J., and Strobbia, C.: Surface wave methods for near-surface site characterization, CRC
517 Press, ISBN: 9781138077737, 2015.

518 Giardino, J.R., Vitek, J.D., and Demorett, J.L.: A model of water movement in rock glaciers and associated water
519 characteristics, in: *Periglacial Geomorphology*, edited by: Dixon, J.C., and Abrahams, A.D., Routledge, London,
520 159-184, <https://doi.org/10.4324/9781003028901-7>, 1992.

521 Glazer, M., Dobński, W., Marciak, A., Majdański, M., and Błaszczyk, M.: Spatial distribution and controls of
522 permafrost development in non-glacial Arctic catchment over the Holocene, Fuglebekken, SW Spitsbergen,
523 *Geomorphology*, 358, 107128, <https://doi.org/10.1016/j.geomorph.2020>, 2020.

524 Guillemot, A., Helmstetter, A., Larose, E., Baillet, L., Garambois, S., Mayoraz, R., and Delaloye, R.: Seismic
525 monitoring in the Gugla rock glacier (Switzerland): ambient noise correlation, microseismicity and modeling,
526 *Geophysical Journal International*, 221 (3), 1719–1735, <https://doi.org/10.1093/gji/ggaa097>, 2020.

527 Guillemot, A., Baillet, L., Garambois, S., Bodin, X., Helmstetter, A., Mayoraz, R., and Larose, E.: Modal
528 sensitivity of rock glaciers to elastic changes from spectral seismic noise monitoring and modelling, *The
529 Cryosphere*, 15, 501–529, <https://doi.org/10.5194/tc-15-501-2021>, 2021.

530 Haeberli, W.: Untersuchungen zur Verbreitung von Permafrost zwischen Flüelapass und Piz Graletsch
531 (Graubünden), *Mitteilung der Versuchsanstalt für Wasserbau, Hydrologie und Glaziologie*, ETH Zurich, Zurich,
532 1975.

533 Haeberli, W., Kääb, A., Wagner, S., Mühl, D. V., Geissler, P., Haas, J. N., ... and Wagenbach, D.: Pollen analysis
534 and 14C age of moss remains in a permafrost core recovered from the active rock glacier Murtèl-Corvatsch, Swiss
535 Alps: geomorphological and glaciological implications, *Journal of Glaciology*, 45(149), 1-8,
536 <https://doi.org/10.3189/S002214300002975>, 1999.

537 Haeberli, W., Hallet, B., Arenson, L., Elconin, R., Humlum, O., Kääb, A., and Mühl, D. V.: Permafrost creep
538 and rock glacier dynamics, *Permafrost and Periglacial Processes*, 17(3), 189-214, <https://doi.org/10.1002/ppp.561>,
539 2006.

540 Hauck, C., and Kneisel, C.: *Applied Geophysics in Periglacial Environments*, Cambridge University Press., 2008.

541 Hauck, C., Böttcher, M., and Maurer, H.: A new model for estimating subsurface ice content based on combined
542 electrical and seismic data sets, *The Cryosphere*, 5, 453–468, <https://doi.org/10.5194/tc-5-453-2011>, 2011.

543 Herrmann, R. B.: *Computer Programs in Seismology*, St Louis University, 1987.

544 Hu, Y., Arenson, L. U., Barboux, C., Bodin, X., Cicoira, A., Delaloye, R., Gärtner-Roer, I., Kääb, A., Kellerer-
545 Pirkbauer, A., Lambiel, C., Liu, L., Pellet, C., Rouyet, L., Schoeneich, P., Seier, G., and Strozzi, T.: Rock Glacier
546 Velocity: An Essential Climate Variable Quantity for Permafrost, *Reviews of Geophysics*, 63, e2024RG000847,
547 <https://doi.org/10.1029/2024RG000847>, 2025.

548 Janke, J.R., Regmi, N.R., Giardino, J.R., and Vitek, J.D.: Rock glaciers, in: *Treatise on Geomorphology*, Elsevier
549 Inc., Amsterdam, The Netherlands, 238–273, <https://doi.org/10.1016/B978-0-444-63369-9.00012-4>, 2013.

550 Jacquemart, M., Weber, S., Chiarle, M., Chmiel, M., Cicoira, A., Corona, C., Eckert, N., Gaume, J., Giacoma, F.,
551 Hirschberg, J., Kaitna, R., Magnin, F., Mayer, S., Moos, C., van Herwijnen, A., and Stoffel, M.: Detecting the
552 impact of climate change on alpine mass movements in observational records from the European Alps, *Earth-
553 Science Reviews*, 258, 104886, <https://doi.org/10.1016/j.earscirev.2024.104886>, 2024.

554 Jones, D. B., Harrison, S., Anderson, K., and Whalley, W. B.: Rock glaciers and mountain hydrology: A review,
555 *Earth-Science Reviews*, 193, 66–90, <https://doi.org/10.1016/j.earscirev.2019.04.001>, 2019.

556 Kellerer-Pirkbauer, A., Bodin, X., Delaloye, R., Lambiel, C., Gärtner-Roer, I., Bonnefoy-Demongeot, M., ... and
557 Zumiani, M.: Acceleration and interannual variability of creep rates in mountain permafrost landforms (rock
558 glacier velocities) in the European Alps in 1995–2022, *Environmental Research Letters*, 19(3), 034022,
559 <https://doi.org/10.1088/1748-9326/ad25a4>, 2024.

560 Kenner, R., Phillips, M., Hauck, C., Hilbich, C., Mulsow, C., Bühl, Y., ... and Buchroithner, M.: New insights
561 on permafrost genesis and conservation in talus slopes based on observations at Flüelapass, Eastern Switzerland,
562 *Geomorphology*, 290, 101-113, <https://doi.org/10.1016/j.geomorph.2017.04.011>, 2017.

563 Kenner, R., Noetzli, J., Hoelzle, M., Raetzo, H., and Phillips, M.: Distinguishing ice-rich and ice-poor permafrost
564 to map ground temperatures and ground ice occurrence in the Swiss Alps. *The Cryosphere*, 13(7), 1925-1941,
565 <https://doi.org/10.5194/tc-13-1925-2019>, 2019.

566 Kenner, R., Pruessner, L., Beutel, J., Limpach, P., and Phillips, M.: How rock glacier hydrology, deformation
567 velocities and ground temperatures interact: Examples from the Swiss Alps, *Permafrost Periglac*, 31, 3–14,
568 <https://doi.org/10.1002/ppp.2023>, 2020.

569 Kofler, C., Mair, V., Gruber, S., Todisco, M. C., Nettleton, I., Steger, S., ... and Comiti, F.: When do rock glacier
570 fronts fail? Insights from two case studies in South Tyrol (Italian Alps), *Earth Surface Processes and Landforms*,
571 46(7), 1311-1327, <https://doi.org/10.1002/esp.5099>, 2021.

572 Krainer, K. and Mostler, W.: Hydrology of Active Rock Glaciers: Examples from the Austrian Alps, Arctic,
573 Antarctic, and Alpine Research, 34, 142–149, <https://doi.org/10.1080/15230430.2002.12003478>, 2002.

574 Krainer, K., Mostler, W., and Spötl, C.: Discharge from active rock glaciers, Austrian Alps: a stable isotope
575 approach, *Austrian Journal of Earth Sciences*, 100, 102-112, 2007.

576 Krainer, K., Bressan, D., Dietre, B., Haas, J. N., Hajdas, I., Lang, K., ... and Tonidandel, D.: A 10,300-year-old
577 permafrost core from the active rock glacier Lazaun, southern Ötztal Alps (South Tyrol, northern Italy),
578 *Quaternary Research*, 83(2), 324-335, <https://doi.org/10.1016/j.yqres.2014.12.005>, 2015.

579 Kuehn, T., Holt, J. W., Johnson, R., and Meng, T.: Active seismic refraction, reflection, and surface wave surveys
580 in thick debris-covered glacial environments, *Journal of Geophysical Research: Earth Surface*, 129,
581 e2023JF007304, <https://doi.org/10.1029/2023JF007304>, 2024.

582 Kula, D., Olszewska, D., Dobiński, W., and Glazer, M.: Horizontal-to-vertical spectral ratio variability in the
583 presence of permafrost, *Geophysical Journal International*, 214, 219–231, <https://doi.org/10.1093/gji/ggy118>,
584 2018.

585 Lerjen, M., Kääb, A., Hoelzle, M., and Haeberli, W.: Local distribution pattern of discontinuous mountain
586 permafrost. a process study at Flüela Pass, Swiss Alps, in: *Proceedings of the 8th International Conference on*
587 *Permafrost*, Zurich, Switzerland, 667-672, ISBN: 90 5809 582 7, 2003.

588 Liu, H., Maghoul, P., and Shalaby, A.: Seismic physics-based characterization of permafrost sites using surface
589 waves, *The Cryosphere*, 16, 1157–1180, <https://doi.org/10.5194/tc-16-1157-2022>, 2022.

590 Mair, V., Zischg, A., Lang, K., Tonidandel, D., Krainer, K., Kellerer-Pirklbauer, A., ... and Böckli, L.: PermaNET-
591 Permafrost Long-term Monitoring Network. Synthesis report (Vol. 1), International Research Society
592 INTERPRAEVENT, ISBN 978-3-901164-14-9, 2011.

593 Noetzli, J., Isaksen, K., Barnett, J., Christiansen, H. H., Delaloye, R., Etzelmüller, B., ... and Phillips, M.: Enhanced warming of European mountain permafrost in the early 21st century, *Nature Communications*, 15(1),
594 1-15, <https://doi.org/10.1038/s41467-024-54831-9>, 2024.

596 Olafsdottir, E. A., Bessason, B., Erlingsson, S., and Kaynia, A. M.: A Tool for Processing and Inversion of MASW
597 Data and a Study of Inter-session Variability of MASW, *Geotechnical Testing Journal*, 47(5), 1006-1025,
598 <https://doi.org/10.1520/GTJ20230380>, 2024.

599 Park, C. B., Miller, R. D., and Xia, J.: Multichannel analysis of surface waves, *Geophysics*, 64(3), 800808,
600 <https://doi.org/10.1190/1.1444590>, 1999.

601 Park, C. B., Miller, R. D., Xia, J., and Ivanov, J.: Multichannel analysis of surface waves (MASW) - active and
602 passive methods, *The Leading Edge*, 26(1), 60-64, <https://doi.org/10.1190/1.2431832>, 2007.

603 Park, C., Richter, J., Rodrigues, R., and Cirone, A.: MASW applications for road construction and maintenance,
604 *The Leading Edge*, 37(10), 724-730, <https://doi.org/10.1190/tle37100724.1>, 2018.

605 Pavoni, M., Carrera, A., and Boaga, J.: Improving the galvanic contact resistance for geoelectrical measurements
606 in debris areas: A case study, *Near Surface Geophysics*, 20(2), 178-191, <https://doi.org/10.1002/nsg.12192>, 2022.

607 Pavoni, M., Boaga, J., Carrera, A., Zuecco, G., Carturan, L., and Zumiani, M.: Brief communication: Mountain
608 permafrost acts as an aquitard during an infiltration experiment monitored with electrical resistivity tomography
609 time-lapse measurements, *The Cryosphere*, 17, 1601–1607, <https://doi.org/10.5194/tc-17-1601-2023>, 2023a.

610 Pavoni, M., Boaga, J., Wagner, F. M., Bast, A., and Phillips, M.: Characterization of rock glaciers environments
611 combining structurally-coupled and petrophysically-coupled joint inversions of electrical resistivity and seismic
612 refraction datasets, *Journal of Applied Geophysics*, 215, 105097, <https://doi.org/10.1016/j.jappgeo.2023.105097>,
613 2023b.

614 Petersson, N.A., and Sjögren, B.: User's guide to SW4, version 3.0, LLNL-SM-741439 (LLNL-SM-741439),
615 2023.

616 PERMOS 2020: Swiss Permafrost Bulletin 2018/2019. Pellet, C. and Noetzli, J. (eds.), 20 pp.,
617 doi.org/10.13093/permos-bull-2020, 2020.

618 Phillips, M., Mutter, E. Z., Kern-Luetschg, M., and Lehning, M.: Rapid degradation of ground ice in a ventilated
619 talus slope: Flüela Pass, Swiss Alps, *Permafrost Periglac.*, 20, 1–14, <https://doi.org/10.1002/ppp.638>, 2009.

620 Phillips, M., Buchli, C., Weber, S., Boaga, J., Pavoni, M., and Bast, A.: Brief communication: Combining
621 borehole temperature, borehole piezometer and cross-borehole electrical resistivity tomography measurements to
622 investigate seasonal changes in ice-rich mountain permafrost, *The Cryosphere*, 17, 753–760,
623 <https://doi.org/10.5194/tc-17-753-2023>, 2023.

624 Picotti, S., Carcione, J. M., Germán Rubino, J., and Santos, J. E.: P-wave seismic attenuation by slow-wave
625 diffusion: Numerical experiments in partially saturated rocks, *Geophysics*, 72(4), N11-N21,
626 <https://doi.org/10.1190/1.2740666>, 2007.

627 Pride, S.R., Berryman, J.G., and Harris, J.M.: Seismic attenuation due to wave-induced flow, *Journal of*
628 *Geophysical Research*, 109, B01201, <https://doi.org/10.1029/2003JB002639>, 2004.

629 RGIK. Towards standard guidelines for inventorying rock glaciers: baseline concepts (version 4.2.2), IPA Action
630 Group Rock glacier inventories and kinematics, 13 pp, 2022.

631 Rücker, C., Günther, T., and Wagner, F. M.: pyGIMLi: An open-source library for modelling and inversion in
632 geophysics, *Computers & Geosciences*, 109, 106-123, <https://doi.org/10.1016/j.cageo.2017.07.011>, 2017.

633 Sambridge, M.: Geophysical inversion with a neighbourhood algorithm: I. Searching a parameter space,
634 *Geophysical Journal International*, 138(2), 479–494, <https://doi.org/10.1046/j.1365-246X.1999.00876.x>, 1999.

635 Scott, W. J., Sellmann, P., and Hunter, J. A.: Geophysics in the study of permafrost, *Geotechnical and*
636 *environmental geophysics*, 1, 355-384, <https://doi.org/10.1190/1.9781560802785.ch13>, 1990.

637 Shi Z., He X., Chen D., and Wang X.: Seismic wave dispersion and attenuation resulting from multiscale wave-
638 induced fluid flow in partially saturated porous media, *Geophysical Journal International*, 236, 1172–1182,
639 <https://doi.org/10.1093/gji/ggad475>, 2024.

640 Sjögreen, B., and Petersson, N.A.: A Fourth Order Accurate Finite Difference Scheme for the Elastic Wave
641 Equation in Second Order Formulation, *Journal of Scientific Computing*, 52(1), 17-48,
642 <https://doi.org/10.1007/s10915-011-9531-1>, 2012.

643 Socco, L. V., Foti, S. and Boiero, D.: Surface-wave analysis for building near-surface velocity models -
644 Established approaches and new perspectives, *Geophysics*, 75(5), 75A83–75A102,
645 <https://doi.org/10.1190/1.3479491>, 2010.

646 Tourei, A., Ji, X., Rocha dos Santos, G., Czarny, R., Rybakov, S., Wang, Z., Hallissey, M., Martin, E. R., Xiao
647 M., Zhu, T., Nicolsky, D., and Jensen, A.: Mapping Permafrost Variability and Degradation Using Seismic
648 Surface Waves, Electrical Resistivity, and Temperature Sensing: A Case Study in Arctic Alaska, *Journal of*
649 *Geophysical Research: Earth Surface*, 129, e2023JF007352, <https://doi.org/10.1029/2023JF007352>,
650 2024.

651 Wagner, F.M., Mollaret, C., Günther, T., Kemna, A., and Hauck, C.: Quantitative imaging of water, ice and air in
652 permafrost systems through petrophysical joint inversion of seismic refraction and electrical resistivity data,
653 *Geophys. J. Int.*, 219(3), 1866–1875, <https://doi.org/10.1093/gji/ggz402>, 2019.

654 Wathen, M.: An improved neighborhood algorithm: Parameter conditions and dynamic scaling, *Geophysical*
655 *Research Letters*, 35(9), L09301, <https://doi.org/10.1029/2008GL033256>, 2008.

656 Williams, P. J.: Unfrozen Water Content of Frozen Soils and Soil Moisture Suction, *Géotechnique*, 14, 231–246,
657 <https://doi.org/10.1680/geot.1964.14.3.231>, 1964.

658 Zhang, L., Wang, S., and Petersson, N.A.: Elastic Wave Propagation in Curvilinear Coordinates with Mesh
659 Refinement Interfaces by a Fourth Order Finite Difference Method, *SIAM J. Sci. Comp.*, 43(2), A1472-A1496,
660 <https://doi.org/10.1137/20M1339702>, 2021.